metals

MDPI

Article

Effects of Heat Treatment on Microstructures and Corrosion Properties of $Al_xCrFeNi$ Medium-Entropy Alloy

Pushan Guo [1,*], Yuan Pang [1], Qingke Zhang [2,*], Lijing Yang [2], Zhenlun Song [2] and Yi Zhang [1]

[1] School of Mechanical Engineering and Rail Transit, Changzhou University, Changzhou 213164, China; pangyuan@nimte.ac.cn (Y.P.); zy@cczu.edu.cn (Y.Z.)
[2] Key Laboratory of Marine Materials and Related Technologies, Zhejiang Key Laboratory of Marine Materials and Protective Technologies, Ningbo Institute of Materials Technology and Engineering, Chinese Academy of Sciences, Ningbo 315201, China; yanglj@nimte.ac.cn (L.Y.); songzhenlun@nimte.ac.cn (Z.S.)
* Correspondence: guopushan@cczu.edu.cn (P.G.); zhangqingke@nimte.ac.cn (Q.Z.); Tel.: +86-188-9261-5697 (P.G.); +86-0574-86685893 (Q.Z.)

Abstract: This study designed $Al_xCrFeNi$ (x = 0.8, 1.0, 1.2) medium-entropy alloys featuring a BCC + B2 dual-phase structure to systematically investigate the effects of Al content variation and heat treatment on microstructure evolution and corrosion behavior. Microstructural characterization revealed that all investigated alloys maintained the BCC + B2 dual-phase labyrinth structure. Electrochemical tests showed that as the Al content increased, the corrosion current density and corrosion rate in a 3.5 wt% NaCl solution increased. Synergistic analysis of post-corrosion morphology (through electrochemical testing and in-situ immersion) combined with XPS analysis of the passive films revealed that the initial stage of corrosion was primarily pitting. Subsequently, due to the loose and porous Al_2O_3 passive layer formed by the NiAl-rich phase, which was easily attacked by Cl^- ions, the corrosion progressed into selective corrosion of the NiAl phase. Notably, heat treatment at 1000 °C induced microstructural refinement with enhanced coupling between chunky and labyrinth structures, resulting in improved corrosion resistance despite a 4–6% reduction in Vickers hardness due to elemental homogenization. Among the investigated alloys, the heat-treated $Al_{0.8}CrFeNi$ exhibited the most promising corrosion resistance.

Keywords: $Al_xCrFeNi$; medium-entropy alloys; microstructure; corrosion behavior; heat treatment

check for updates

Academic Editor: Seok Su Sohn

Received: 13 February 2025
Revised: 3 March 2025
Accepted: 6 March 2025
Published: 7 March 2025

Citation: Guo, P.; Pang, Y.; Zhang, Q.; Yang, L.; Song, Z.; Zhang, Y. Effects of Heat Treatment on Microstructures and Corrosion Properties of $Al_xCrFeNi$ Medium-Entropy Alloy. *Metals* **2025**, *15*, 292. https://doi.org/10.3390/met15030292

Copyright: © 2025 by the authors. Licensee MDPI, Basel, Switzerland. This article is an open access article distributed under the terms and conditions of the Creative Commons Attribution (CC BY) license (https://creativecommons.org/licenses/by/4.0/).

1. Introduction

High-entropy alloys (HEAs) have garnered significant research attention owing to their innovative design concepts and excellent properties. Pioneering work by Cantor and Yeh [1,2] established HEAs as multi-principal-element alloys with equiatomic or near-equiatomic compositions (5–35 at.% range). As derivatives of HEAs, medium-entropy alloys (MEAs) are characterized by either 2–4 principal elements or a configurational entropy of 1R–1.5R [3–5]. Similar to HEAs, MEAs manifest four fundamental effects: high entropy, sluggish diffusion, severe lattice distortion, and cocktail effects [6]. These synergistic effects endow MEAs with outstanding mechanical properties, including high strength, elevated hardness, and superior wear and corrosion resistance [7–10]. The properties of alloys can be controlled by adjusting the types and ratios of elements to adapt to different application scenarios. In this context, Zhou et al. designed $AlCoCrFeNiTi_x$ (x = 0, 0.5, 1, 1.5) high-entropy alloys with five or more elements as the main components, different from traditional alloys [11]. This alloy system is primarily composed of body-centered cubic

solid solution and has excellent room-temperature compressive properties. This breakthrough propelled the AlCoCrFeNi system to the forefront of HEA research. Due to the scarcity of cobalt, the difficulty of extraction, and high demand, its price remains high in the international metal trading market. According to the trading prices on the London Metal Exchange, the minimum trading price of cobalt in 2024 is about 21,500 USD/ton, which is significantly higher than nickel at 15,000 USD/ton, aluminum at 2100 USD/ton, chromium at 8500 USD/ton, and iron at 100 USD/ton. To promote the industrial application of this alloy, Hillel et al. investigated the effects of the elements in AlCoCrFeNi alloy and found that Fe and Co exert a similar effect of minimization of crystallographic mismatch between the BCC and B2 phases. Additionally, AlCrFeNi resembles the most quinary AlCoCrFeNi alloy in terms of microstructure and mechanical properties [12]. Regarding synthesis methods, Jiang et al. prepared AlCrFeNi samples through three different synthesis methods and conducted tests [13]. All samples prepared by these synthesis methods are found to exhibit relatively high yield strength (>1040 MPa) and failure strain (>28%). Thus, the industrial application of AlCrFeNi medium-entropy alloys with excellent mechanical properties, which reduce cost by lowering cobalt content, is possible. Some studies have attempted further to optimize the components and properties of the AlCrFeNi alloys. Liu et al. designed $Al_{25-x}Cr_{25+0.5x}Fe_{25}Ni_{25+0.5x}$ (x = 19 at.%, 17 at.%, 15 at.%) and found that increased Al content can increase the volume fraction of BCC phase, improve strength, and reduce plasticity [14]. Wang et al. reported that heat treatment and increased Al content promote the transformation of the original FCC + BCC phase into a BCC + B2 phase in the AlCrFeNi alloy system [15], and the existence of a double strengthening phase (BCC + B2) also ensures the mechanical properties of alloys. Researchers have concentrated mostly on the impact of the composition content and heat treatment on AlCrFeNi medium-entropy alloys in the aspects of mechanical properties and microstructure, whereas corrosion resistance is rarely investigated. To address this gap, we designed Al_xCrFeNi medium-entropy alloys with different Al contents (x = 0.8, 1.0, 1.2) and treated them at 1000 °C for 1 h, systematically investigating the combined effects of Al content and heat treatment on microstructure evolution, hardness, and corrosion resistance in 3.5 wt% NaCl solution.

2. Materials and Methods

2.1. Material Preparation

Al_xCrFeNi medium-entropy alloys (x = 0.8, 1.0, 1.2) were prepared by arc melting, using elements of Al, Cr, Fe, and Ni with purities of more than 99.9% as raw materials in a high-purity Ar atmosphere on a vacuum arc-melting furnace (Kejingzhida, Shenzhen, China). At smelting temperatures of 1200–1300 °C, the alloy ingot was flipped and melted eight times, with a duration of 3 min each time. Electromagnetic stirring was conducted. After the melting was completed, the ingot was produced by casting the melt into an ingot with dimensions of 50 mm × 50 mm × 5 mm after slow cooling to room temperature. The specimens for the following tests with different dimensions were cut from these alloys by electro-discharge machining. The samples were subjected to X-ray fluorescence spectrometry (Bruker, Karlsruhe, Germany) to detect their Nominal and actual compositions, as summarized in Table 1. The ingots were treated at 1000 °C at a heating rate of 25 °C·min^{-1} and preserved for 1 h under Ar atmosphere, followed by furnace cooling.

Table 1. Nominal and actual compositions of the as-cast $Al_xCrFeNi$ medium entropy alloys.

Element	$Al_{0.8}CrFeNi$		$Al_{1.0}CrFeNi$		$Al_{1.2}CrFeNi$	
	Nominal	**Measured**	**Nominal**	**Measured**	**Nominal**	**Measured**
Al	21.05	21.65	25	25.29	28.57	28.88
Cr	26.31	25.64	25	24.14	23.81	22.96
Fe	26.31	25.55	25	24.82	23.81	23.25
Ni	26.31	27.16	25	25.75	23.81	24.91

2.2. Microstructural Characterization and Composition Analysis

After preparation, the surfaces of these samples were wet abraded through a series of silicon carbide papers, polished on cloth by using 1.5 μm diamond pastes, cleaned with ethanol, and rinsed with sterile distilled water to remove contaminants. The morphologies of samples were investigated using a scanning electron microscope (Carl Zeiss AG, Oberkochen, Germany) with an energy-dispersive spectrometer. The samples were etched with dilute aqua regia to examine the microstructure under an optical microscope (Oupu, Ningbo, China). An X-ray diffractometer (Bruker, Karlsruhe, Germany) was used to analyze the phase composition of the samples by using a Cu-Kα radiation source having a 2θ scope of 10° to 100° at a scanning velocity of $6°\cdot min^{-1}$. X-ray fluorescence spectrometry was used to identify the element content.

2.3. Microhardness Test

After grinding and polishing the samples until no obvious scratches were visible on the surface, the samples were ultrasonically cleaned using anhydrous ethanol, and microhardness testing was performed on the cleaned sample surface under a load of 1000 g for 15 s on a Vickers hardness tester (Gaoxie, Suzhou, China). Five measurements were made for each sample, and the averaged experimental data were obtained. Five indentations were made at an adequate distance from previous indentations for all samples.

2.4. Corrosion Properties

2.4.1. Electrochemical Tests

Electrochemical tests were performed using an electrochemical workstation (Metrohm, Herisau, Switzerland). A three-electrode configuration was used for electrochemical measurements; platinum plate, saturated calomel electrode, and as-prepared samples served as the counter, reference, and working electrodes, respectively. The potential was swept from Eocp−0.5 V to Eocp+1 V, and the polarization curves were recorded at a scan rate of 1 $mV\cdot s^{-1}$. From the anodic and cathodic polarization curves, the Tafel regions were identified and extrapolated to the corrosion potential (E_{corr}) to obtain the corrosion current density (J_{corr}). Other parameters were analyzed using Nova software (1.11, Metrohm, Herisau, Switzerland). The corroded surface of the samples after the potentiodynamic polarization measurement in a 3.5 wt% NaCl corrosive solution was observed by scanning electron microscopy (Carl Zeiss AG, Oberkochen, Germany).

2.4.2. In-Situ Immersion Corrosion Tests and XPS Characterizations

The samples were immersed in a 3.5 wt% NaCl corrosive solution and soaked at room temperature for 0, 3, 7, and 15 days. After different immersion times, the samples were taken out from the solution, cleaned with deionized water, and subjected to SEM (Carl Zeiss AG, Oberkochen, Germany) to observe the corrosion surface at the same location. The compositions of the passive film were determined by XPS (Thermo Fisher Scientific, Waltham, MA, USA). The analysis-chamber pressure was 1×10^{-9} mBar, and the excitation source used was Al Kα radiation (hv = 1486.68 eV), with an X-ray spot size of 400 μm. The

operating voltage was 15 kV, and the filament current was 10 mA. The test passing energy was set to 30 eV, with a step size of 0.1 eV. Charging correction was performed using C 1s (284.80 eV) binding energy as the reference.

3. Results and Discussion

3.1. Microstructural Characteristics

As shown in the XRD patterns in Figure 1, $Al_xCrFeNi$ alloys under as-cast and heat-treated conditions, comprising a Cr-Fe phase solid solution with a disordered BCC structure and a NiAl phase intermetallic compound with an ordered B2 structure. The superposition of diffraction peaks coinciding in the XRD pattern, which comprised the (110), (200), and (211) planes, primarily resulted from the spinodal decomposition. Under the effect of spinodal decomposition, the crystal structures of the two phases were the same. Their lattice parameters were similar as well [16]. Some ultra-strong coincide peaks in the as-cast and heat-treated $Al_{1.0}CrFeNi$ alloys were attributed to the increase in large radius atomic (Al) content that initiated the pinning effect and lattice distortion [17]. Additionally, the coincident peaks of BCC + B2 phases at (211) planes slightly shifted to lower angles in as-cast and heat-treated $Al_{1.2}CrFeNi$ alloys. For the as-cast condition, the peak position shifted from 81.5 to 81.2; for the heat-treated condition, the peak shifted from 81.9 to 81.5. This shift was attributed to the increased Al content in the phase that reflected the larger atomic-size effect of Al atoms in expanding the BCC and B2 structures [18].

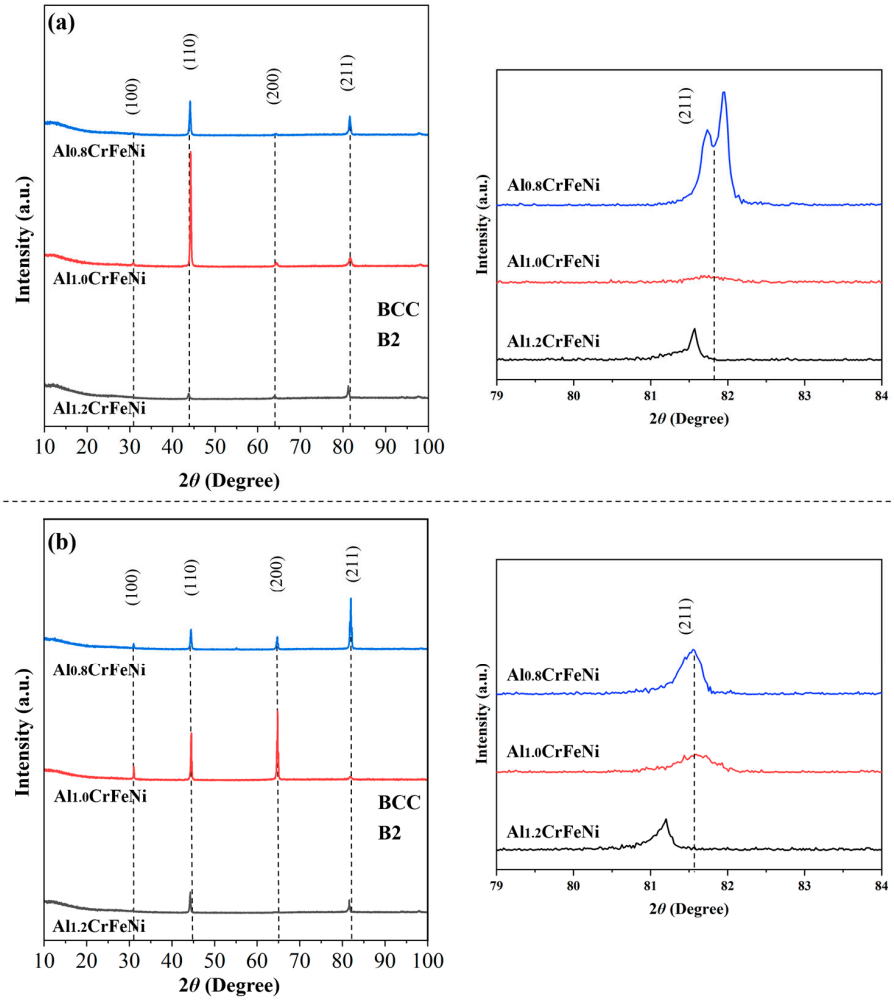


Figure 1. The XRD pattern and partially enlarged view of (**a**) as-cast and (**b**) heat-treated $Al_xCrFeNi$ Medium entropy alloys.

The optical microscopy images of the microstructures of $Al_xCrFeNi$ alloys under as-cast and heat-treated conditions are presented in Figure 2. Under the as-cast condition, the $Al_{0.8}CrFeNi$ alloy primarily exhibited dendritic structures with non-uniform grain sizes and coarse eutectic structures along grain boundaries. For $Al_{1.0}CrFeNi$ alloy, the microstructure transitioned to equiaxed grains having improved size uniformity, accompanied by the eutectic structures around the grain boundaries becoming more compact and the labyrinthine eutectic structures in the grain centers becoming denser. In $Al_{1.2}CrFeNi$ alloy, due to the typical Ostwald ripening effect [19], the grain morphology became disordered, the eutectic structures around the grain boundaries disappeared, and the chunky element-enriched structures precipitated in the grain centers coupled with the labyrinth structure. Compared with the as-cast condition, heat-treated $Al_{0.8}CrFeNi$ alloy showed a dense lamellar structure at the grain boundaries likely due to the elemental precipitation caused by heat treatment. In heat-treated $Al_{1.0}CrFeNi$ alloy, the grain boundaries became blurred and showed a tendency toward integration, with smaller grain sizes and denser labyrinth structures in the grain centers. For $Al_{1.2}CrFeNi$ alloy, heat treatment further refined grain sizes while strengthening the coupling between chunky and labyrinth structures.

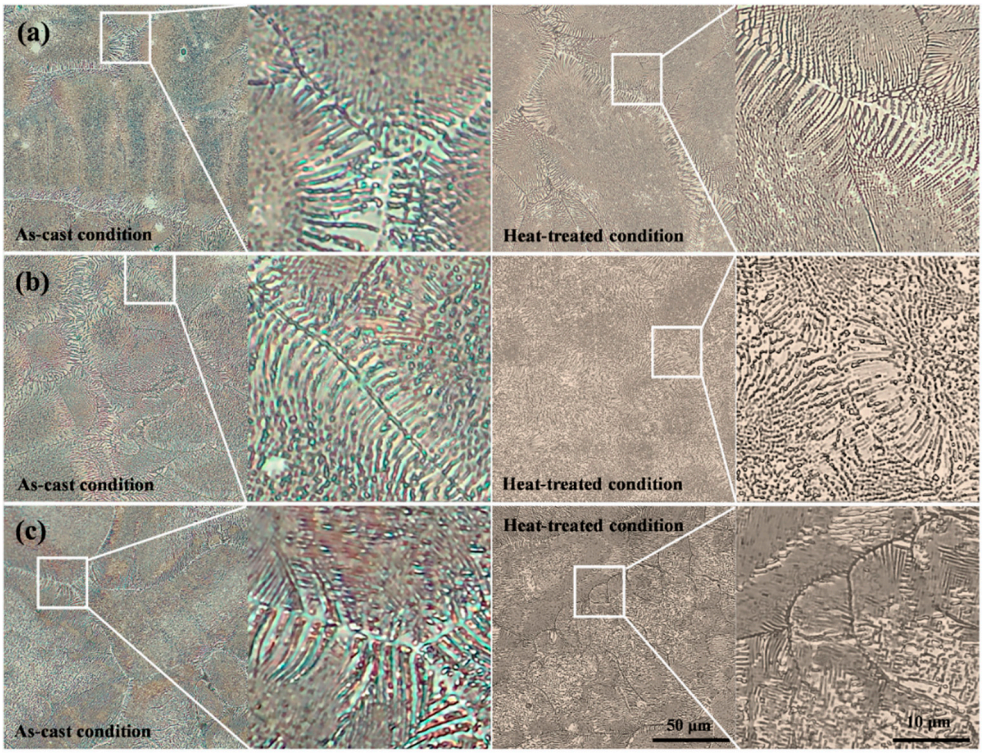


Figure 2. The microstructure of (**a**) $Al_{0.8}CrFeNi$, (**b**) $Al_{1.0}CrFeNi$, and (**c**) $Al_{1.2}CrFeNi$ medium entropy alloy.

The BS-SEM images of $Al_xCrFeNi$ medium-entropy alloys and the compositions of the different phases determined by EDS are presented in Figure 3. Results indicated that these regions exhibited two phases: dark gray phase and light gray phase. Microprobe microanalysis showed that Al and Ni elements were enriched in the dark gray phase, and Cr and Fe elements were enriched in the light gray phase, corresponding with the B2 and BCC phases, respectively. As presented in Figure 3b, the labyrinth structure of as-cast $Al_{1.0}CrFeNi$ was rounder than that of as-cast $Al_{0.8}CrFeNi$, which can be ascribed to the synergistic impact for lattice distortion and Ostwald Ripening effect. A new chunky structure appeared and coupled with the labyrinth structure in $Al_{1.2}CrFeNi$ alloy. Post heat treatment (1000 °C), the MEAs exhibited significant microstructural refinement. The

labyrinth structure of $Al_xCrFeNi$ alloys after heat treatment was finer than that under as-cast conditions. The chunky structure of $Al_{1.2}CrFeNi$ became smaller and more closely coupled with the labyrinth structure. Overall, the microstructure achieved improved uniformity, indicating the effective phase homogenization via thermal processing.

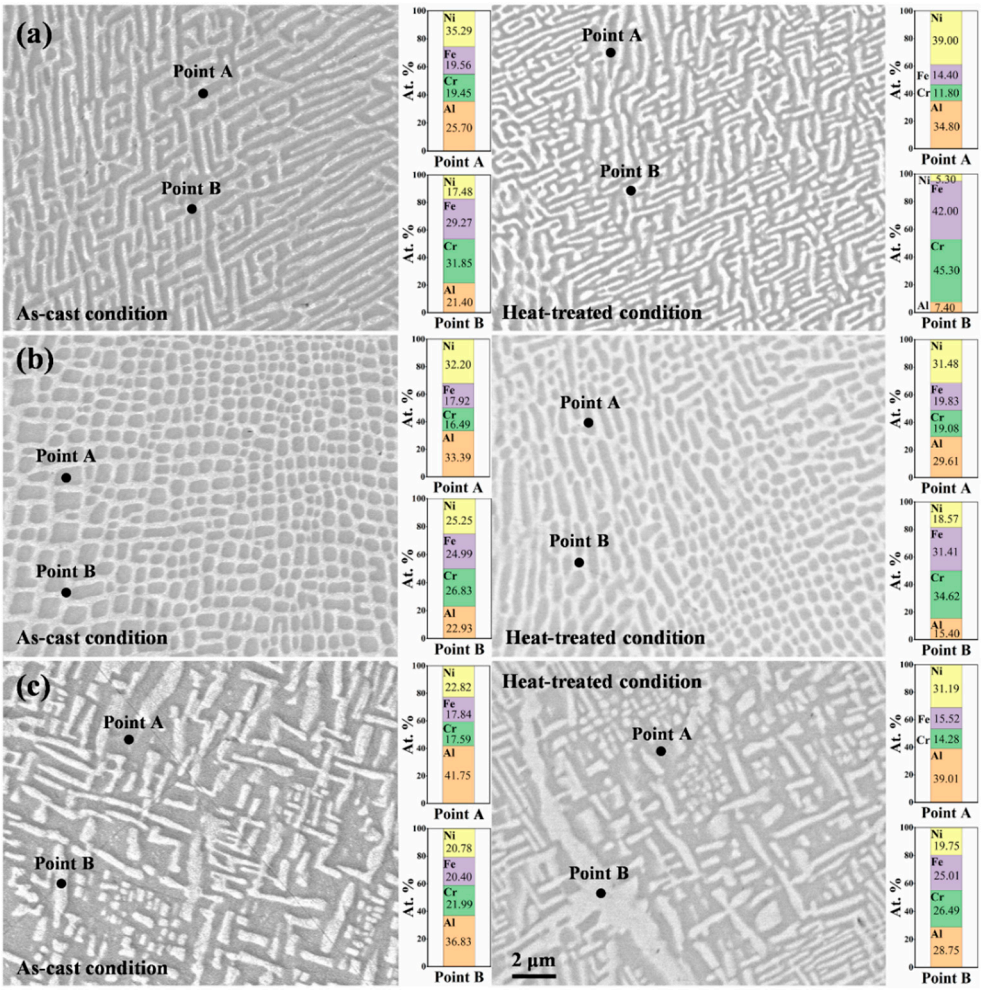


Figure 3. Backscattered SEM images and phase elements proportion of (**a**) $Al_{0.8}CrFeNi$, (**b**) $Al_{1.0}CrFeNi$, and (**c**) $Al_{1.2}CrFeNi$ medium-entropy alloy.

3.2. Microhardness Property

The microhardness of $Al_xCrFeNi$ (x = 0.8, 1.0, 1.2) alloys was tested using a Vickers hardness tester under a 1000 g load. As shown in Table 2, the increased Al content in the alloy resulted in an enhancement of microhardness, whereas the heat-treated samples exhibited lower hardness than their as-cast counterparts. These three kinds of alloys consisted of two phases, namely, BCC and B2 (ordered BCC). The BCC structure has a relatively larger free volume and greater atomic spacing, which makes dislocation motion easier in the BCC structures, leading to easier deformation. In contrast, the alternating elements in the B2 structure and the stronger atomic bonding restrict dislocation motion more, thereby increasing hardness. As the Al content increases, the volume fraction of the NiAl phase with a B2 structure in the alloy gradually increases, leading to a continuous improvement in the hardness of the alloys. From a microscopic structural perspective, the increase in Al content influenced the material's mechanical properties in two ways: solid-solution strengthening and grain-refinement strengthening. The added Al, in addition to combining with Ni to form the B2 (NiAl) phase, also dissolved into the BCC (FeCr) solid solution. However, compared with other elements like Cr and Fe, Al had the largest atomic

radius. When Al solute atoms dissolved into the solid solution, significant lattice distortion occurred to minimize the system's overall energy. At this stage, the dislocation pinning effect may impede dislocation motion, thereby contributing to increased hardness [16].

Table 2. Microhardness of as-cast and heat-treated Al_xCrFeNi alloys.

Sample		Hardness ($HV_{1.0}$)	Sample		Hardness ($HV_{1.0}$)
As-cast condition	$Al_{0.8}$CrFeNi	457.9	Heat-treated condition	$Al_{0.8}$CrFeNi	431.06
	$Al_{1.0}$CrFeNi	462.4		$Al_{1.0}$CrFeNi	439.38
	$Al_{1.2}$CrFeNi	466.96		$Al_{1.2}$CrFeNi	451.02

3.3. Corrosion Properties

The potentiodynamic polarization curves of Al_xCrFeNi alloys in a 3.5 wt% NaCl solution are shown in Figure 4. According to existing research, the AlCoCrFeNi alloy containing Co exhibits a corrosion potential of −0.435 V, a corrosion current density of 8.27×10^{-5} A/cm^2, a pitting potential of −0.01 V, and a corrosion rate of 0.74 mm/year in 3.5 wt.% NaCl solution [20]. In comparison, the cobalt-free AlCrFeNi alloy demonstrates superior corrosion parameters in polarization tests and enhanced corrosion resistance. The corrosion parameters obtained from Tafel plots in the active area are summarized in Table 3. Both the corrosion current density (J_{corr}) and corrosion rate increased with Al addition, implying poorer corrosion resistance of $Al_{1.2}$CrFeNi alloy. Furthermore, the decrease in critical pitting potential (E_p) indicated that the increase in Al content led to a decrease in localized corrosion resistance. E_p is defined as the potential at which the current density passes 10^{-4} A/cm^2 and continues to increase. Consequently, E_p can serve as an indicator of resistance to localized corrosion [21]. By comparing the corrosion parameters of the alloys before and after heat treatment, we observed that the corrosion current density (J_{corr}) and corrosion rate decreased, and the critical pitting potential (E_p) increased. This finding indicated that heat treatment improved both the corrosion resistance and localized corrosion resistance in a 3.5 wt% NaCl corrosive solution. This improvement was attributed to the uniform distribution of elements and the reduction in element enrichment caused by heat treatment. Additionally, as illustrated by the curves, all Al_xCrFeNi alloys directly transitioned from the Tafel region to the stable passive region without any active-to-passive transition, suggesting the spontaneous formation of a protective film at the corrosion potential [22].

Table 3. Polarization parameters of as-cast and heat-treated Al_xCrFeNi alloys in 3.5 wt% NaCl corrosive solution.

Sample		E_{corr}/(V)	J_{corr}/(A/cm^2)	E_p/(V)	Corrosion Rate (mm/year)
As-cast condition	$Al_{0.8}$CrFeNi	−0.38	4.7×10^{-7}	0.11	0.011
	$Al_{1.0}$CrFeNi	−0.39	6.1×10^{-7}	0.10	0.015
	$Al_{1.2}$CrFeNi	−0.35	1.1×10^{-6}	0.06	0.026
Heat-treated condition	$Al_{0.8}$CrFeNi	−0.36	3.6×10^{-7}	0.15	0.004
	$Al_{1.0}$CrFeNi	−0.33	4.3×10^{-7}	0.14	0.010
	$Al_{1.2}$CrFeNi	−0.42	4.8×10^{-7}	0.07	0.012

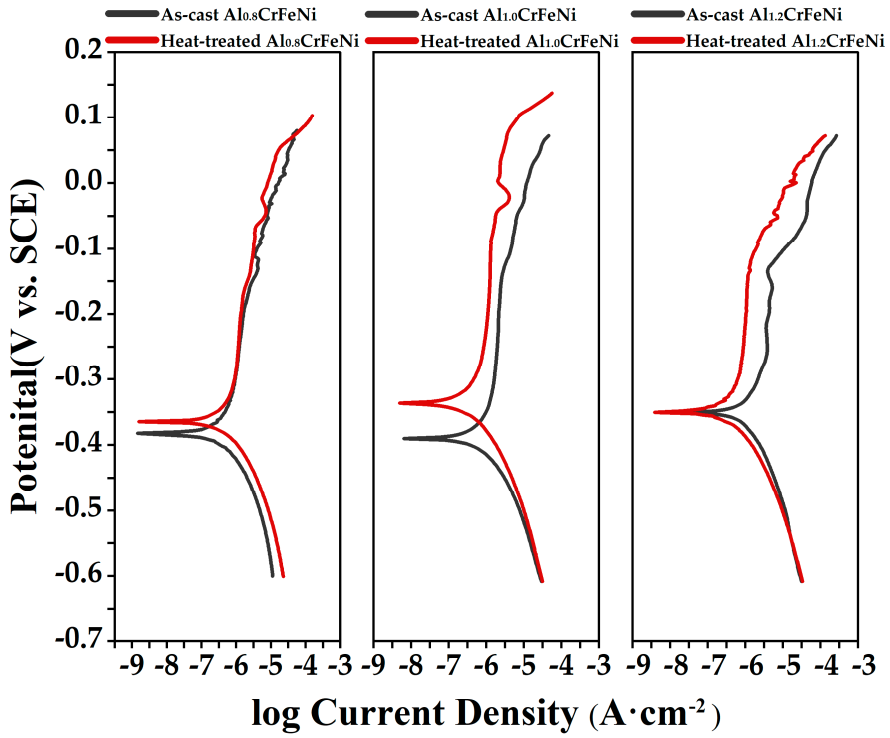


Figure 4. Potentiodynamic polarization curves of as-cast and heat-treated $Al_xCrFeNi$ alloys in 3.5 wt% NaCl corrosive solution.

The Backscattered SEM surface morphologies of $Al_xCrFeNi$ alloys were studied after electrochemical tests in a 3.5 wt% NaCl corrosive solution, and the results are shown in Figure 5. All alloys suffered from selective corrosion, with the dark gray phase dissolved, whereas the light gray phase was nearly intact. Based on the microstructure analysis above, we concluded that the dark gray phase corresponded to the NiAl (B2) phase and the light gray phase to the CrFe (BCC) phase. In alloy systems, chromium exhibits a propensity to form a dense Cr_2O_3 passive film, which demonstrates superior resistance to chloride ion (Cl^-) penetration, thereby significantly enhancing the corrosion resistance of the CrFe phase. In contrast, the NiAl phase, enriched with aluminum, develops a surface Al_2O_3 film. However, the Al_2O_3 film displays compromised stability in chloride-containing environments, where it readily reacts with Cl^- ions to form soluble aluminum chloride ($AlCl_3$). This reaction mechanism induces localized breakdown of the passive film, serving as initiation sites for pitting corrosion. Chloride ions exhibit a pronounced tendency to adsorb at surface defects of the NiAl phase, particularly at grain boundaries and dislocations. This adsorption facilitates localized acidification through passive film penetration, characterized by proton (H^+) accumulation, which subsequently catalyzes metallic ion hydrolysis to establish a self-accelerating corrosive microenvironment. Furthermore, the chemical interaction between aluminum and chloride ions generates soluble corrosion products (e.g., $AlCl_3$) [23], resulting in progressive degradation of the passive film and inward propagation of corrosion fronts, ultimately forming distinct pitting cavities. Following pit nucleation at NiAl phase surfaces, corrosive attack preferentially propagates along phase boundaries or grain boundaries. This phenomenon is exacerbated by the ordered B2 (NiAl) intermetallic structure, which inherently promotes compositional heterogeneity and residual stress concentrations at these interfacial regions, thereby creating preferential pathways for chloride-assisted degradation. Consequently, corrosion channels dominated by NiAl phase dissolution are systematically established. In contrast, the CrFe phase maintains significantly lower corrosion rates due to the electrochemical stability of its passive film. This differential corrosion behavior creates a microscale sacrificial-protection

mechanism, wherein the anodic NiAl phase preferentially corrodes while the cathodic CrFe phase remains electrochemically protected. The detailed analysis of the composition of the passivation layer is described in the XPS section. By comparing the sections after heat treatment in Figure 6, the corrosion on the surface of the samples prior to heat treatment was found to be more severe than that observed after treatment. This disparity was attributed to the homogenization effect of the heat treatment, which increased the volume fraction of the BCC phase and reduced the element enrichment, thereby significantly minimizing localized corrosion and enhancing corrosion resistance. This finding aligns with the results obtained from the polarization curves. As shown in Figure 6a–c, with increased Al content to 28.57 at.% ($Al_{1.2}$CrFeNi), the severity of corrosion significantly escalated. This escalation was attributed to the higher Al content, which exacerbated element segregation and led to the formation of chunky NiAl phase-rich structures with uneven element distribution.

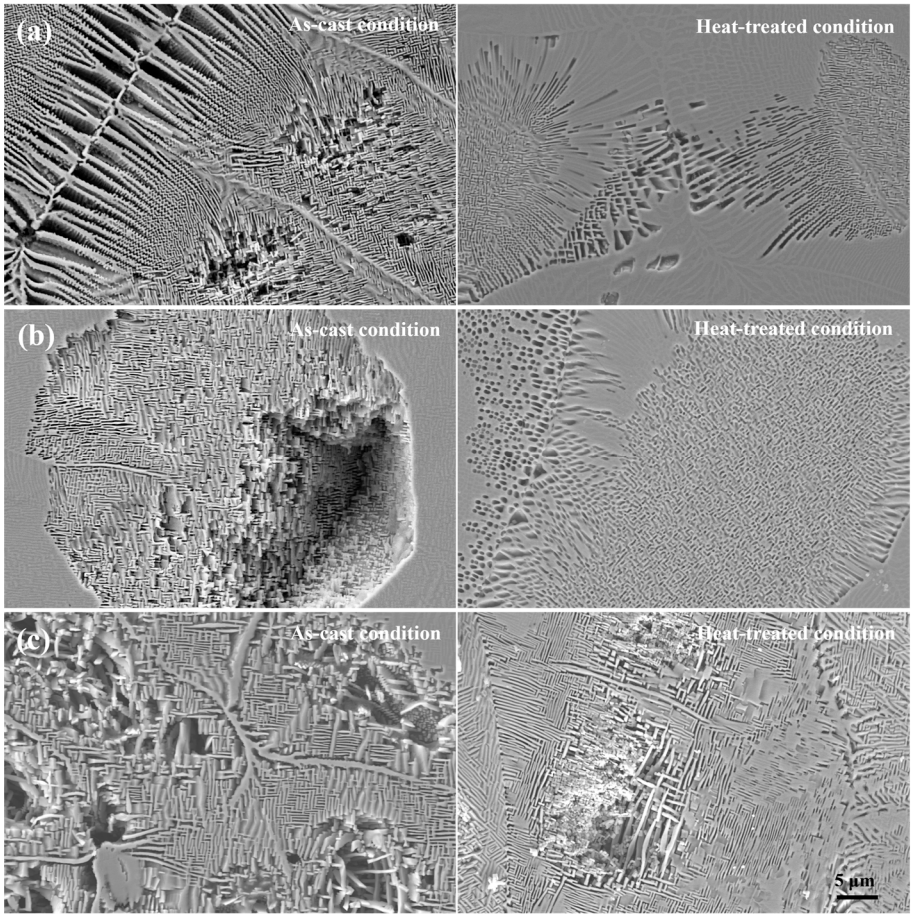


Figure 5. Backscattered SEM surface morphologies of (**a**) $Al_{0.8}$CrFeNi, (**b**) $Al_{1.0}$CrFeNi, and (**c**) $Al_{1.2}$CrFeNi medium entropy alloy after potentiodynamic polarization in 3.5 wt% NaCl corrosive solution at room temperature.

Figure 6 presents the in-situ immersion corrosion morphology of the as-cast Al_xCrFeNi alloys in a 3.5 wt% NaCl corrosive solution. As shown in Figure 6, $Al_{0.8}$CrFeNi had no pitting corrosion for up to 15 days, with only corrosion products forming. Conversely, $Al_{1.0}$CrFeNi began to show pitting corrosion in 15 days, and $Al_{1.2}$CrFeNi began to show pitting corrosion in 7 days, respectively. Moreover, by day 15, the number of pits on $Al_{1.2}$CrFeNi increased, and the existing pits expanded. These observations align with the results from the potentiodynamic polarization tests, confirming that the corrosion resistance of the alloy decreases as the Al content increases. Combined with the corrosion morphology obtained from the potentiodynamic polarization experiment (Figure 5), pitting

corrosion is revealed as the predominant mechanism in the early stages of corrosion. The higher aluminum content leads to an increased proportion of Al_2O_3 in the passive film. Compared to Cr_2O_3, the crystalline structure of Al_2O_3 is more prone to forming defects such as grain boundaries and dislocations. These defects serve as preferential pathways for Cl^- adsorption and penetration. Furthermore, chromium (Cr) is a critical element for the self-repairing capability of the passive film (where Cr^{3+} migrates to defect sites and re-oxidizes into Cr_2O_3). Elevated aluminum content dilutes the Cr concentration in the alloy, thereby reducing the film repair rate. Once pitting nucleation occurs, it propagates rapidly to form pitting pits [24]. Within these pits, hydrolysis of metal cations (Al^{3+}, Cr^{3+}, Fe^{2+}, etc.) generates H^+ ions, resulting in localized pH reduction. Notably, Al^{3+} exhibits a higher hydrolysis tendency, which intensifies acidification. This process accelerates Cl^- migration and metal dissolution, ultimately exacerbating pitting corrosion development [25].

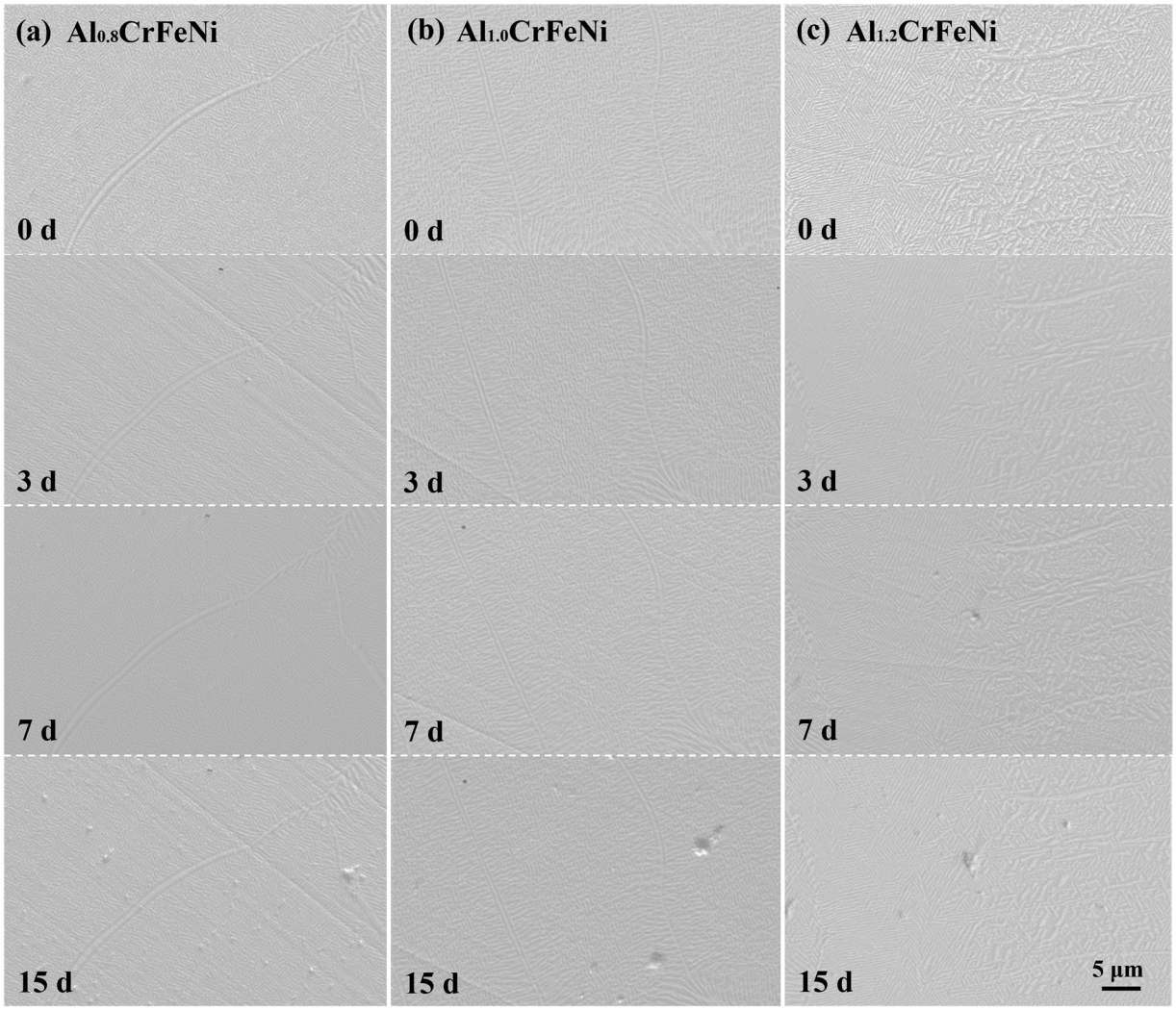


Figure 6. In-situ immersion corrosion morphologies of the as-cast (**a**) $Al_{0.8}CrFeNi$, (**b**) $Al_{1.0}CrFeNi$, and (**c**) $Al_{1.2}CrFeNi$ medium-entropy alloy immersed in 3.5 wt% NaCl corrosive solution at room temperature for 0 d, 3 d, 7 d, and 15 d.

Figure 7 presents the in-situ immersion corrosion morphology of heat-treated $Al_xCrFeNi$ alloys in a 3.5 wt% NaCl corrosive solution. Corrosion pits formed in $Al_xCrFeNi$ alloys after 15 days, with $Al_{1.2}CrFeNi$ exhibiting a significantly higher number and density of pits. This reflected the positive effect of heat treatment on corrosion resistance. The grain refinement induced by heat treatment effectively suppressed the elemental aggre-

gation at the grain boundaries and promoted a more uniform distribution of elements across phases. Cl^- ions attacked lattice defects such as grain boundaries and dislocations when corrosion occurred, leading to oxide-layer formation. After heat treatment, the increased number of grain boundaries and higher dislocation density effectively enhanced the corrosion resistance of the material. The abundance of grain boundaries had higher energy than most of the material, enhancing electron diffusion and leading to a more stable passive film, thereby improving corrosion resistance [26]. The heat treatment effectively eliminates residual stresses, thereby reducing localized stress concentration regions that are prone to passive film rupture, which otherwise promotes Cl^- adsorption and pitting nucleation. Elevated-temperature heat treatment promotes the diffusion of Cr elements, resulting in a homogenized Cr distribution that maintains the proportion of Cr_2O_3 in the passive film. Furthermore, the refined and uniform microstructure accelerates the migration of Cr^{3+}/Fe^{2+} ions to defect sites during corrosion processes, significantly enhancing the self-repair efficiency of the passive film and suppressing the propagation of pitting corrosion [27].

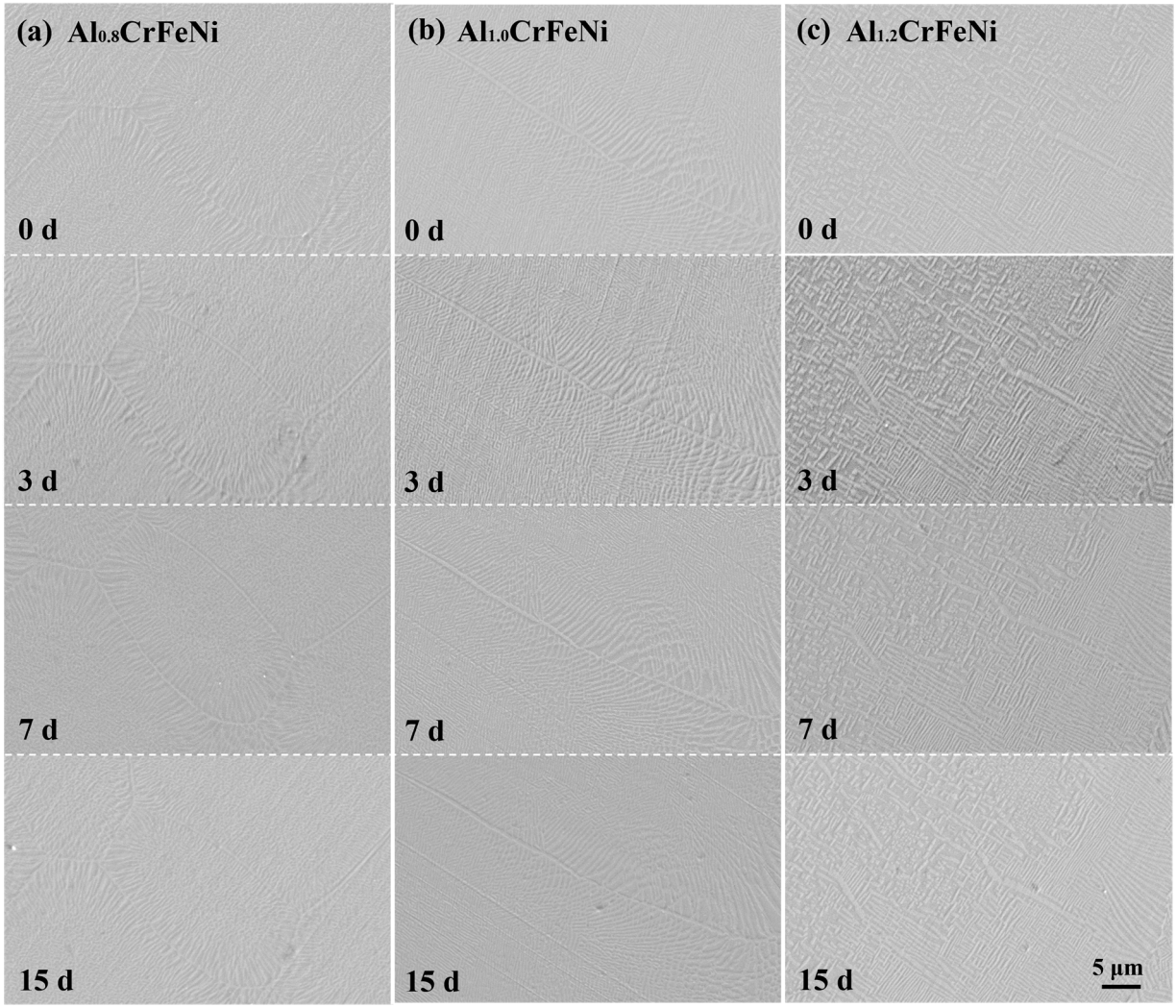


Figure 7. In-situ immersion corrosion morphologies of the heat-treated (**a**) $Al_{0.8}CrFeNi$, (**b**) $Al_{1.0}CrFeNi$, and (**c**) $Al_{1.2}CrFeNi$ medium-entropy alloy immersed in 3.5 wt% NaCl corrosive solution at room temperature for 0 d, 3 d, 7 d, and 15 d.

XPS was used to analyze the chemical composition and elemental valence states of the passive film formed on the surface of samples after 15 days of immersion in a 3.5 wt%

NaCl corrosive solution to explore the passivation mechanism of the alloys in greater detail. The findings are illustrated in Figures 8 and 9. Clearly, the Al 2p spectrum was divided into two component peaks: the metallic state Al^0 (72.48 and 74.43 eV) and the oxidized state Al_{ox}^{3+} (73.03 eV). This finding indicated that Al_2O_3 was the primary oxide product of Al in the passive film. The Cr 2p spectrum showed three component peaks, namely, Cr^0 (574.28 and 583.6 eV), Cr_{ox}^{3+} (576.48 and 586.16 eV), and Cr_{hy}^{3+} (577.89 and 587.75 eV), with Cr_2O_3 playing a critical role [28]. The Fe 2p spectrum also contains three component peaks: Fe^0 (707.03 ev and 719.84 eV), Fe_{ox}^{2+} (709.17 and 721.97 ev), and Fe_{ox}^{3+} (711.79 and 725.01 eV). In aqueous environments, reactions lead to the formation of FeO, Fe_2O_3, and Fe_3O_4. FeO, being the most reactive among them, undergoes further oxidation, yielding Fe_2O_3 and Fe_3O_4 [29]. The Ni 2p spectrum revealed Ni^0 (852.84 and 871.02 eV), Ni_{ox}^{2+} (855.66 and 873.58 eV), and Ni_{sat} (861.77 and 879.72 eV) as its three component peaks. Comparing the spectra of Fe and Ni with those of Al and Cr, the peak intensities clearly demonstrated that Fe and Ni were less prone to oxidation. Additionally, the O 1s spectrum revealed three key peaks: O^{2-} (530.48 eV), OH^- (531.89 eV), and H_2O (533.35 eV). O^{2-} actively facilitated the formation of Al_2O_3, Cr_2O_3, Fe_2O_3, FeO, Fe_3O_4, and NiO [30]. Meanwhile, OH^- was primarily responsible for the formation of $Cr(OH)_3$, and bound water enhanced the capture of dissolved metal ions, promoting the growth and stability of the passive film [31]. In aqueous environments, the electrochemical corrosion of metals typically progresses through two primary stages: the anodic oxidation and dissolution of the metal and the cathodic reduction of anions. As the metal lost electrons, it formed cations that reacted with anions, producing insoluble compounds on the substrate surface. This process resulted in active metal dissolution, reduced surface area, and a barrier against further ion intrusion, effectively impeding continued corrosion. Al is a highly reactive metal that readily forms complexes with halogen atoms. Cl^- ions in the solution compromise the integrity of the dense Al_2O_3 film, increasing the solubility of Al^{3+} and accelerating the corrosion and dissolution of the alloy substrate [32]. During the early stages of corrosion, a passivation film forms on the NiAl-rich surface, effectively impeding corrosion. Over time, the oxidation of Ni and Al generates H^+ ions, which accumulate in the adjacent solution. The increased concentration of H^+ ions promotes the dissolution of Ni^{2+} and Al^{3+} into the solution, causing the dissolution rate of the passivation film to surpass its formation rate. Ultimately, the alloy's corrosion resistance is compromised. This phenomenon was further exacerbated by the increased Al content, which amplified the enrichment of the NiAl phase, thereby diminishing the alloy's resistance to corrosion. This effect was particularly pronounced with higher Al content because the intensified enrichment of the NiAl phase further deteriorated the alloy's resistance to corrosion. The diagram in Figure 10 illustrates the corrosion mechanism of Al_xCrFeNi medium-entropy alloys in 3.5 wt% NaCl corrosive solution, and the chemical reaction equations governing the ions within the passivation layer were as follows [33,34]:

$$Al + H_2O \rightarrow AlOH + H^+ + e^- \quad (1)$$

$$AlOH \rightarrow Al(OH)^+ + e^- \quad (2)$$

$$Al(OH)^+ \rightarrow Al(OH)^{2+} + e^- \quad (3)$$

$$Al(OH)^{2+} + H^+ \rightarrow Al^{3+} + H_2O \quad (4)$$

$$2Al + 3H_2O \rightarrow Al_2O_3 + 6H^+ + 6e^- \quad (5)$$

$$2Al + 3H_2O \rightarrow Al_2O_3 + 6H^+ + 6e^- \quad (6)$$

$$2Cr + 3H_2O \rightarrow Cr_2O_3 + 6H^+ + 6e^- \quad (7)$$

$$2Fe+3H_2O \rightarrow Fe_2O_3 + 6H^+ + 6e^- \quad (8)$$

$$Ni+ 2H_2O \rightarrow NiO+4H^+ + 4e^- \quad (9)$$

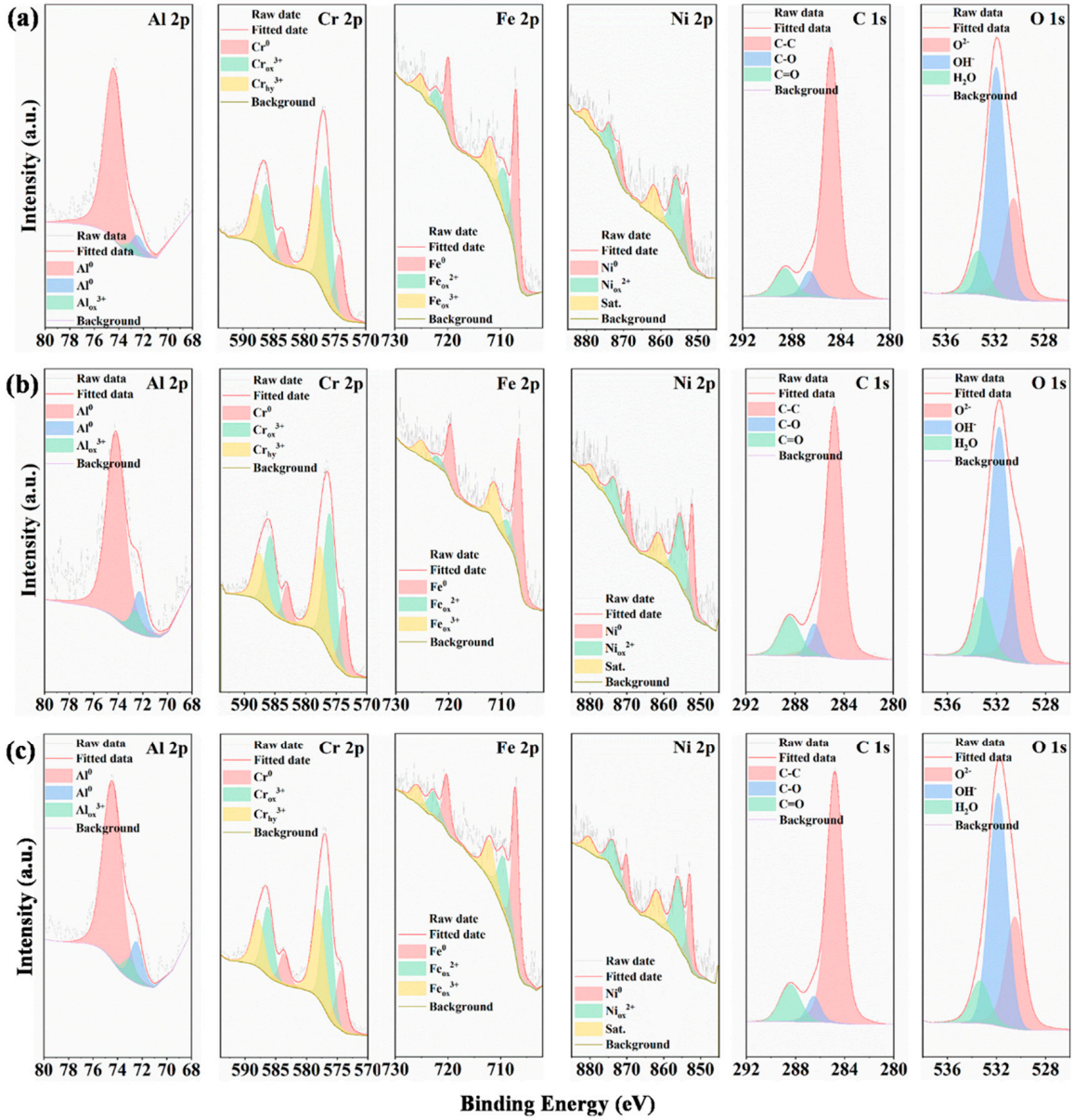


Figure 8. High-resolution XPS spectra of Al 2p, Cr 2p, Fe 2p, Ni 2p, C 1s, and O 1s of passive film on the surfaces of the as-cast (**a**) $Al_{0.8}$CrFeNi, (**b**) $Al_{1.0}$CrFeNi, and (**c**) $Al_{1.2}$CrFeNi medium entropy alloy immersed in 3.5 wt% NaCl corrosive solution for 15 d.

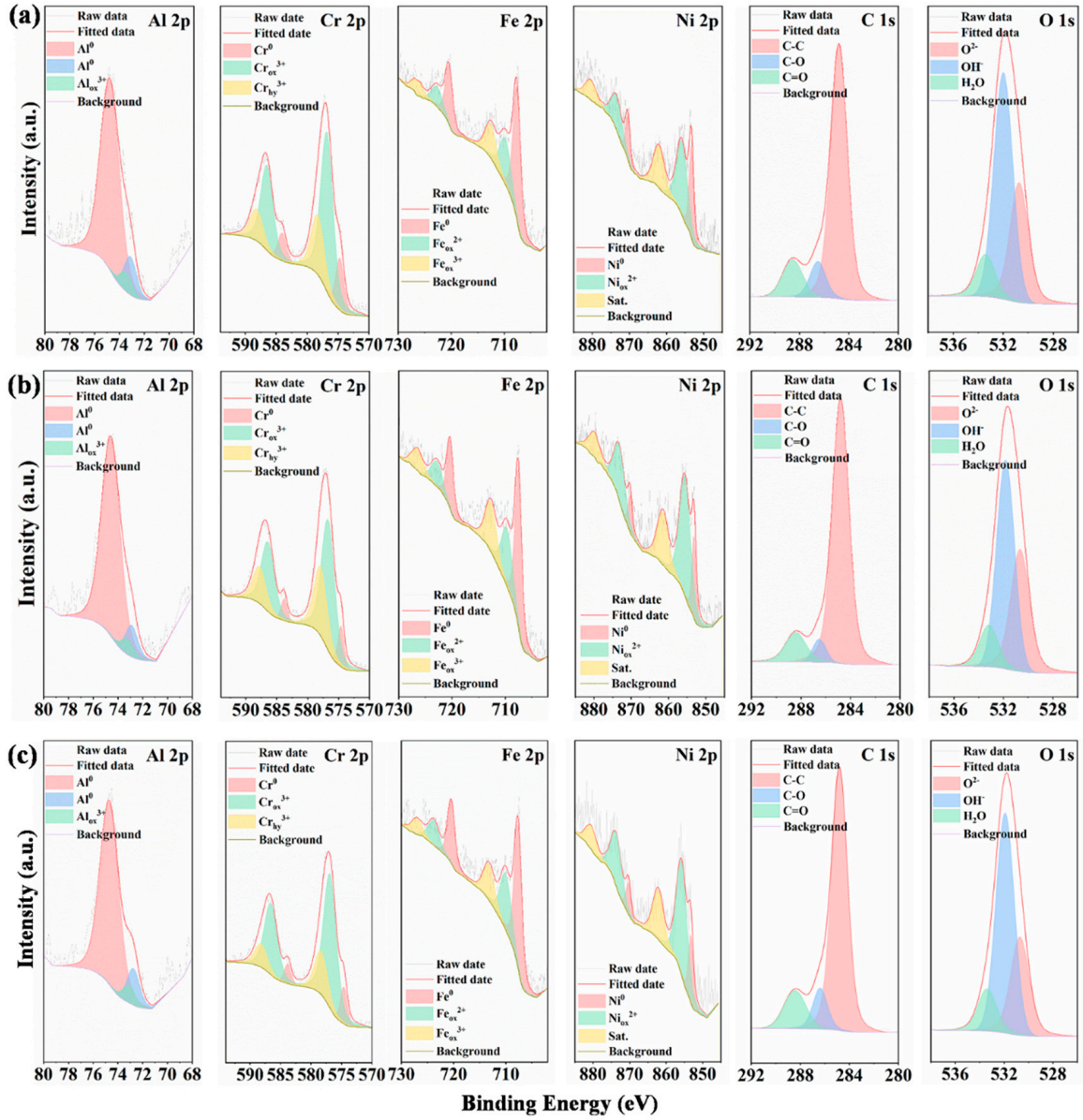


Figure 9. High-resolution XPS spectra of Al 2p, Cr 2p, Fe 2p, Ni 2p, C 1s, and O 1s of passive film on the surfaces of the heat-treated (**a**) $Al_{0.8}CrFeNi$, (**b**) $Al_{1.0}CrFeNi$, and (**c**) $Al_{1.2}CrFeNi$ medium-entropy alloy immersed in 3.5 wt% NaCl solution for 15 d.

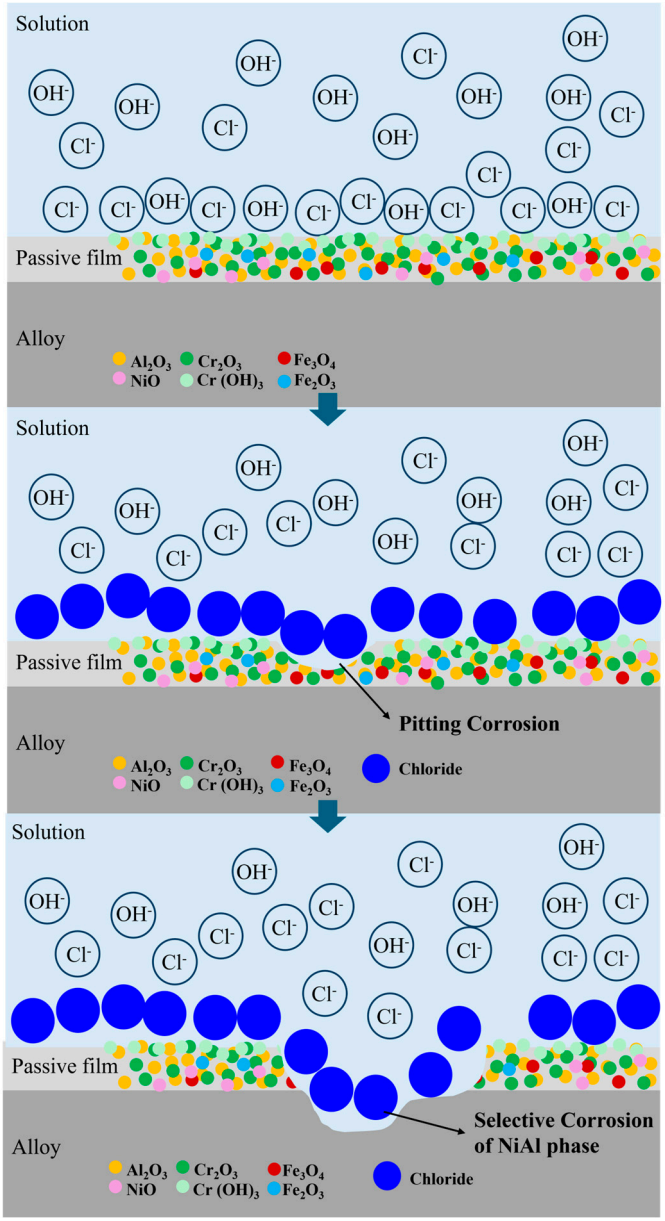


Figure 10. Schematic of the corrosion mechanism of $Al_xCrFeNi$ medium-entropy alloys in 3.5 wt% NaCl corrosive solution.

4. Conclusions

The effects of Al content and heat treatment on the microstructure, mechanical properties, and corrosion resistance in a 3.5 wt% NaCl solution of $Al_xCrFeNi$ (x = 0.8, 1.0, 1.2) alloys were investigated. Our conclusions are as follows.

(1) Before and after heat treatment, the phase composition of the $Al_xCrFeNi$ alloys consisted of a disordered BCC phase and an ordered B2 phase. The BCC and B2 phases interlace to form a labyrinth structure, which becomes more rounded as the Al content increases.

(2) The increase in Al content, which has a larger atomic radius, intensifies element segregation. This causes lattice distortion and dislocation pinning effects, thereby increasing the alloy's hardness. However, heat treatment promoted element homogenization, which reduced the alloy's microhardness.

(3) Increased Al content negatively affects the corrosion resistance of $Al_xCrFeNi$ alloys, whereas heat treatment improves their corrosion resistance.

On the whole, this heat-treated cobalt-free $Al_{0.8}$CrFeNi alloy, like the commonly studied AlCoCrFeNi alloy, has excellent mechanical properties and corrosion resistance while also being more cost-effective. It holds promise for industrial applications in the petrochemical industry.

Author Contributions: Conceptualization, P.G., Y.P. and Y.Z.; Methodology, P.G., Q.Z. and L.Y.; Software, Y.P.; Validation, P.G. and Y.P.; Formal analysis, Q.Z., L.Y. and Z.S.; Investigation, Y.P. and Y.Z.; Resources, P.G. and Z.S.; Data curation, P.G. and Y.P.; Writing—original draft, Y.P.; Writing—review and editing, P.G.; Visualization, P.G. and Y.P.; Supervision, Q.Z. and Y.Z.; Project administration, P.G., Q.Z., L.Y., Z.S. and Y.Z.; Funding acquisition, P.G. All authors have read and agreed to the published version of the manuscript.

Funding: This research was funded by the Natural Science Foundation of Jiangsu Province (No. BK20231339) and the Changzhou Science and Technology Bureau Project (No. CQ20230095).

Data Availability Statement: The raw data supporting the conclusions of this article will be made available by the authors on request.

Conflicts of Interest: The authors declare no financial or commercial conflicts of interest.

References

1. Cantor, B.; Chang, I.T.H.; Knight, P.; Vincent, A.J.B. Microstructural development in equiatomic multicomponent alloys. *Mater. Sci. Eng. A* **2004**, *375–377*, 213–218. [CrossRef]
2. Yeh, J.-W.; Chen, S.-K.; Lin, S.-J.; Gan, J.-Y.; Chin, T.-S.; Shun, T.-T.; Tsau, C.-H.; Chang, S.-Y. Nanostructured High-Entropy Alloys with Multiple Principal Elements: Novel Alloy Design Concepts and Outcomes. *Adv. Eng. Mater.* **2004**, *6*, 299–303. [CrossRef]
3. Castro, D.; Jaeger, P.; Baptista, A.C.; Oliveira, J.P. An Overview of High-Entropy Alloys as Biomaterials. *Metals* **2021**, *11*, 648. [CrossRef]
4. Coury, F.G.; Zepon, G.; Bolfarini, C. Multi-principal element alloys from the CrCoNi family: Outlook and perspectives. *J. Mater. Res. Technol.-JmrT* **2021**, *15*, 3461–3480. [CrossRef]
5. Miracle, D.B.; Miller, J.D.; Senkov, O.N.; Woodward, C.; Uchic, M.D.; Tiley, J. Exploration and Development of High Entropy Alloys for Structural Applications. *Entropy* **2014**, *16*, 494–525. [CrossRef]
6. Miracle, D.B.; Senkov, O.N. A critical review of high entropy alloys and related concepts. *Acta Mater.* **2017**, *122*, 448–511. [CrossRef]
7. Tsai, C.-W.; Tsai, M.-H.; Yeh, J.-W.; Yang, C.-C. Effect of temperature on mechanical properties of $Al_{0.5}$CoCrCuFeNi wrought alloy. *J. Alloys Compd.* **2010**, *490*, 160–165. [CrossRef]
8. Shi, T.; Lei, P.-H.; Yan, X.; Li, J.; Zhou, Y.-D.; Wang, Y.-P.; Su, Z.-X.; Dou, Y.-K.; He, X.-F.; Yun, D.; et al. Current development of body-centered cubic high-entropy alloys for nuclear applications. *Tungsten* **2021**, *3*, 197–217. [CrossRef]
9. Todai, M.; Nagase, T.; Hori, T.; Matsugaki, A.; Sekita, A.; Nakano, T. Novel TiNbTaZrMo high-entropy alloys for metallic biomaterials. *Scr. Mater.* **2017**, *129*, 65–68. [CrossRef]
10. Aly, H.A.; Abdelghafar, K.A.; Gaber, G.A.; Mohamed, L.Z. Fabrication, Characterization, and Corrosion Behavior of a New $Cu_{40}Mn_{25}Al_{20}Fe_5Co_5Ni_5$ High-Entropy Alloy in HNO_3 Solution. *J. Mater. Eng. Perform.* **2021**, *30*, 1430–1443. [CrossRef]
11. Zhou, Y.J.; Zhang, Y.; Wang, Y.L.; Chen, G.L. Solid solution alloys of AlCoCrFeNiTi_x with excellent room-temperature mechanical properties. *Appl. Phys. Lett.* **2007**, *90*, 2734517. [CrossRef]
12. Hillel, G.; Natovitz, L.; Salhov, S.; Haroush, S.; Pinkas, M.; Meshi, L. Understanding the Role of the Constituting Elements of the AlCoCrFeNi High Entropy Alloy through the Investigation of Quaternary Alloys. *Metals* **2020**, *10*, 1275. [CrossRef]
13. Jiang, Z.; Chen, W.; Xia, Z.; Xiong, W.; Fu, Z. Influence of synthesis method on microstructure and mechanical behavior of Co-free AlCrFeNi medium-entropy alloy. *Intermetallics* **2019**, *108*, 45–54. [CrossRef]
14. Liu, M.; Zuo, L.; Li, X.; Li, R.; Zhang, T. Microstructure and Mechanical Properties of $Al_{25-x}Cr_{25+0.5x}Fe_{25}Ni_{25+0.5x}$ (x = 19, 17, 15 at%) Multi-Component Alloys. *Adv. Eng. Mater.* **2018**, *20*, 201701057. [CrossRef]
15. Wang, M.; Wen, Z.; Ma, B.; Liu, J.; Zou, Z.; Zhao, Y. Enhancing the strength of AlCrFeNi HEAs via tailoring aluminum content and optimal aging treatment. *J. Alloys Compd.* **2022**, *893*, 162242. [CrossRef]
16. Chen, X.; Qi, J.Q.; Sui, Y.W.; He, Y.Z.; Wei, F.X.; Meng, Q.K.; Sun, Z. Effects of aluminum on microstructure and compressive properties of Al-Cr-Fe-Ni eutectic multi-component alloys. *Mater. Sci. Eng. Struct. Mater. Prop. Microstruct. Process.* **2017**, *681*, 25–31. [CrossRef]
17. Wang, M.; Wen, Z.; Liu, J.; Ma, B.; Wang, M.; Zou, Z.; Zhao, Y. Labyrinthine structure Al_xCrFeNi ($x \geq 1$) eutectic high entropy alloys with duplex reinforced phases. *J. Alloys Compd.* **2022**, *918*, 165441. [CrossRef]

18. Wang, W.-R.; Wang, W.-L.; Wang, S.-C.; Tsai, Y.-C.; Lai, C.-H.; Yeh, J.-W. Effects of Al addition on the microstructure and mechanical property of $Al_xCoCrFeNi$ high-entropy alloys. *Intermetallics* **2012**, *26*, 44–51. [CrossRef]
19. Bjorklund, S.; Donaghey, L.F.; Hillert, M. Effect of alloying elements on rate of ostwald ripening of cementite in steel. *Acta Metall.* **1972**, *20*, 867. [CrossRef]
20. Garip, Y.; Ergin, N.; Ozdemir, O. Resistance sintering of $CoCrFeNiAl_x$ (x = 0.7, 0.85, 1) high entropy alloys: Microstructural characterization, oxidation and corrosion properties. *J. Alloys Compd.* **2021**, *877*. [CrossRef]
21. Qvarfort, R. Critical pitting temperature-measurements of stainless-steels with an improved electrochemical method. *Corros. Sci.* **1989**, *29*, 987–993. [CrossRef]
22. Shi, Y.; Collins, L.; Feng, R.; Zhang, C.; Balke, N.; Liaw, P.K.; Yang, B. Homogenization of $Al_xCoCrFeNi$ high-entropy alloys with improved corrosion resistance. *Corros. Sci.* **2018**, *133*, 120–131. [CrossRef]
23. Frankel, G.S. Pitting corrosion of metals—A review of the critical factors. *J. Electrochem. Soc.* **1998**, *145*, 2186–2198. [CrossRef]
24. Macdonald, D.D.; Engelhardt, G.R. The Point Defect Model for Bi-Layer Passive Films. In Proceedings of the Symposium on Corrosion General Session Held During the 217th Meeting of the Electrochemical-Society (ECS), Vancouver, BC, Canada, 25–30 April 2010; pp. 123–144.
25. Revie, R.W.; Uhlig, H.H. *Corrosion and Corrosion Control: An Introduction to Corrosion Science and Engineering*; John Wiley & Sons, Inc.: Hoboken, NJ, USA, 2008.
26. Korchef, A.; Kahoul, A. Corrosion Behavior of Commercial Aluminum Alloy Processed by Equal Channel Angular Pressing. *Int. J. Corros.* **2013**, *2013*, 983261. [CrossRef]
27. Li, J.S.; Mao, Q.Z.; Chen, M.; Qin, W.B.; Lu, X.K.; Liu, T.; She, D.S.; Kang, J.J.; Wang, G.; Zhu, X.B.; et al. Enhanced pitting resistance through designing a high-strength 316L stainless steel with heterostructure. *J. Mater. Res. Technol.* **2021**, *10*, 132–137. [CrossRef]
28. Zhao, Q.; Pan, Z.; Wang, X.; Luo, H.; Liu, Y.; Li, X. Corrosion and passive behavior of $Al_xCrFeNi_{3-x}$ (x = 0.6, 0.8, 1.0) eutectic high entropy alloys in chloride environment. *Corros. Sci.* **2022**, *208*, 110666. [CrossRef]
29. Ming, J.; Wu, M.; Shi, J. Passive film modification by concrete carbonation: Re-visiting a corrosion-resistant steel with Cr and Mo. *Cem. Concr. Compos.* **2021**, *123*, 104178. [CrossRef]
30. Wu, H.; Xie, J.; Yang, H.; Sheng, N.; Yang, Y.; Hou, G.; Li, J.; Zhou, Y.; Sun, X. Corrosion behaviors and passive film properties of a newly developed cost-effective AlCrFeNi eutectic high entropy alloy in different corrosive solutions. *Mater. Today Commun.* **2023**, *37*, 107602. [CrossRef]
31. Wang, Z.; Zhang, G.-H.; Fan, X.-H.; Jin, J.; Zhang, L.; Du, Y.-X. Corrosion behavior and surface characterization of an equiatomic CoCrFeMoNi high-entropy alloy under various pH conditions. *J. Alloys Compd.* **2022**, *900*, 163432. [CrossRef]
32. Nascimento, C.B.; Donatus, U.; Ríos, C.T.; Antunes, R.A. Passive film composition and stability of CoCrFeNi and CoCrFeNiAl high entropy alloysin chloride solution. *Mater. Chem. Phys.* **2021**, *267*, 124582. [CrossRef]
33. Zhao, Y.; Zhu, Z.; Shi, W.; Huang, J. Corrosion behaviors of W-doped laser-cladded high-entropy alloy of AlCoCrFeNi in a simulated sulfur-containing seawater environment. *Intermetallics* **2024**, *169*, 108298. [CrossRef]
34. Peng, Y.; Zhou, G.; Han, J.; Li, J.; Zhang, H.; Zhang, S.; Lin, L.; Chen, L.; Cao, X. Effect of Heat Treatment on the Corrosion Resistance of $AlFeCoNiMo_{0.2}$ High-Entropy Alloy in NaCl and H_2SO_4 Solutions. *Metals* **2023**, *13*, 849. [CrossRef]

Disclaimer/Publisher's Note: The statements, opinions and data contained in all publications are solely those of the individual author(s) and contributor(s) and not of MDPI and/or the editor(s). MDPI and/or the editor(s) disclaim responsibility for any injury to people or property resulting from any ideas, methods, instructions or products referred to in the content.